



## Simulation of channel segregation using a two-phase columnar solidification model – Part I: Model description and verification

J. Li <sup>a,b</sup>, M. Wu <sup>a,b,\*</sup>, J. Hao <sup>a</sup>, A. Ludwig <sup>a</sup>

<sup>a</sup> Simulation and Modeling of Metallurgical Processes, Dept. of Metallurgy, Univ. of Leoben, A-8700 Leoben, Austria

<sup>b</sup> Christian Doppler Lab for Advanced Simulation of Solidification and Melting, Dept. of Metallurgy, Univ. of Leoben, A-8700 Leoben, Austria

### ARTICLE INFO

#### Article history:

Received 30 September 2011

Received in revised form 22 December 2011

Accepted 31 December 2011

Available online 24 January 2012

#### Keywords:

Macrosegregation

Channel

Columnar solidification

Multiphase flow

### ABSTRACT

A numerical investigation on the formation of channel segregation using a two-phase columnar solidification model is presented in this two-part paper. Part I includes a model summary and model verification and Part II presents an in-depth discussion and parameter study on the formation mechanisms of channel segregation. The two phases considered in the model are the liquid melt and solid columnar phase. The morphology of the columnar dendrite trunks is approximated by step-wise growing cylinders with constant primary dendrite arm spacing. The columnar dendrites grow from the mold wall following the liquidus isotherm. The growth kinetics of the columnar trunks is governed by diffusion of the rejected solute surrounding the columnar trunks near the solid–liquid interface. The conservation equations for mass, momentum, species and enthalpy are solved for each phase. The permeability of the two-phase mushy zone is treated with the Blake–Kozeny approach. The model is applied in 2D and 3D simulations of segregation in a Sn–10 wt.% Pb benchmark ingot, as defined by Bellet et al. (2009) [1]. The 3D calculations show channel segregation patterns of predominantly discontinuous lamellar structure with a few rod-like channels. A series of 3D simulations with increasing thickness clarify that, with thickness greater than 0.05 m, the influence of the front and back mold walls on the center plane segregation becomes negligible. Thus, the segregation pattern on the center plane in the 3D case can be sufficiently reproduced by computationally inexpensive 2D calculations. Verification was made by comparison with published models and experimental results.

© 2012 Elsevier B.V. All rights reserved.

### 1. Introduction

Channel segregation is one of the most frequently observed segregation patterns in large steel ingots, vacuum-arc remelting or electro-slag remelting ingots [2,3] and similar castings. These segregation defects are often referred to as ‘A’ segregate [4,5] or lamellar- or plume-structured segregate [6,7] in large steel ingots and ‘freckles’ [8,9] in vertically solidified castings.

In the last decades numerous experimental studies in the area of solidification have contributed to the understanding of channel segregation formation [10–12]. McDonald and Hunt [10,11] built an ammonium chloride water system to study the effect of growth conditions and convection on ‘A’ segregate, and were the first to observe that the formation of ‘A’ segregate was directly caused by the extensive fluid motion in the interdendritic region. Sarazin and Hellawell [12] studied channel segregation in three alloy systems (binary Pb–Sn and Pb–Sb, and ternary Pb–Sn–Sb) during unidirectional solidification in base-chilled ingots and found that the

channels originate from flow perturbations, which can be characterized with the Rayleigh number.

Numerical models [13,14] have also significantly contributed to the understanding of macrosegregation, complimenting experimental investigations and providing a view into these opaque flow systems. Shahani et al. [15] studied the effect of natural convection on the formation of macrosegregation in the case of unidirectional solidification of Sn–Pb and Pb–Sn alloys. Their final simulation results indicated a pattern of channel segregates, but their simulations did not provide insight into how channels are formed. Schneider and Beckermann [16] studied the combined effects of microsegregation, mushy zone permeability, thermosolutal convection and contraction flow on macrosegregation during solidification of a Pb–20 wt.% Sn alloy and found that a higher mushy zone permeability causes longer and more vertically oriented channels, while a lower permeability causes shorter and more horizontally oriented channels. Further studies proposed numerical methods and models [14,17–19] to simulate macrosegregation of Pb–Sn alloy systems based on the benchmark of Hebditch and Hunt [20]. To date most numerical investigations of channel segregates have been limited to 2D, with only a few computational attempts made on full 3D geometries [18].

\* Corresponding author at: Simulation and Modeling of Metallurgical Processes, Dept. of Metallurgy, Univ. of Leoben, A-8700 Leoben, Austria. Tel.: +43 3842 4023103; fax: +43 3842 4023102.

E-mail address: [Menghuai.wu@unileoben.ac.at](mailto:Menghuai.wu@unileoben.ac.at) (M. Wu).

## Nomenclature

$c_0$	initial concentration of the alloy (-)	$Q_{\ell s}^D$	energy exchange by heat transfer ( $\text{J m}^{-3} \text{s}^{-1}$ )
$c_\ell, c_s$	species concentration (-)	$Q_{\ell s}^M, Q_s^M$	energy source term due to phase change ( $\text{J m}^{-3} \text{s}^{-1}$ )
$c_\ell^*, c_s^*$	interface equilibrium species concentration (-)	$R_c$	radius of columnar trunk (m)
$C_{\ell s}^M$	species exchange due to phase change ( $\text{kg m}^{-3} \text{s}^{-1}$ )	$R_f$	far field radius of columnar trunk (m)
$c_{\text{mix}}$	mixture concentration (-)	$S_A$	columnar surface concentration ( $\text{m}^{-1}$ )
$c_p^\ell, c_p^s$	specific heat ( $\text{J kg}^{-1} \text{K}^{-1}$ )	$T, T_\ell, T_s$	temperature (K)
$D_\ell$	diffusion coefficient ( $\text{m}^2 \text{s}^{-1}$ )	$T_{\text{ref}}$	reference temperature for enthalpy definition (K)
$d_c$	diameter of columnar trunk (m)	$T_{\text{EXT}}$	external temperature (K)
$f_\ell, f_s$	volume fraction (-)	$t$	time (s)
$g$	gravity ( $\text{m s}^{-2}$ )	$U_{\ell s}^D$	momentum change due to drag force ( $\text{kg m}^{-2} \text{s}^{-2}$ )
$H^*$	volume heat exchange rate between solid and liquid phases ( $\text{W m}^{-3} \text{K}^{-1}$ )	$U_{\ell s}^M$	momentum exchange due to phase change ( $\text{kg m}^{-2} \text{s}^{-2}$ )
$h$	heat transfer coefficient ( $\text{W m}^{-2} \text{K}^{-1}$ )	$\bar{u}_\ell$	velocity vector of the melt ( $\text{m s}^{-1}$ )
$h_\ell, h_s$	enthalpy ( $\text{J kg}^{-1}$ )	$v_{Rc}$	columnar trunk growth velocity ( $\text{m s}^{-1}$ )
$h_\ell^{\text{ref}}, h_s^{\text{ref}}$	enthalpy at reference temperature ( $\text{J kg}^{-1}$ )	$\Phi_{\text{imp}}$	columnar growing surface impingement (-)
$\Delta h_f$	latent heat (heat of fusion) ( $\text{J kg}^{-1}$ )	$\lambda_1$	primary dendrite arm spacing of columnar (m)
$K$	permeability ( $\text{m}^2$ )	$\lambda_2$	second dendrite arm spacing of columnar (m)
$k$	solute partition coefficient (-)	$\rho_\ell, \rho_s$	density ( $\text{kg m}^{-3}$ )
$k_\ell, k_s$	thermal conductivity ( $\text{W m}^{-1} \text{K}^{-1}$ )	$\mu_\ell$	viscosity ( $\text{kg m}^{-1} \text{s}^{-1}$ )
$M_{\ell s}$	solidification mass transfer rate ( $\text{kg s}^{-1} \text{m}^{-3}$ )	$\bar{\tau}_\ell$	stress-strain tensors ( $\text{kg m}^{-1} \text{s}^{-2}$ )
$m$	liquidus slope of the binary phase diagram ( $\text{K (wt.\%)}^{-1}$ )		
$p$	pressure (Pa)	<b>Subscripts</b>	
		$\ell, s$	indicate liquid and solid phases

The formation of channel segregates is a multiphase and multi-scale problem suitably treated with a simplified version of the authors' mixed columnar-equiaxed solidification model [21,22]. In the current paper the presence of equiaxed crystals is neglected. This volume-average model stems from the pioneering work in the field of multiphase solidification by Beckermann et al. [23–25]. Macro-segregation in a Sn–10 wt.% Pb benchmark ingot, as described by Bellet et al. [1], is simulated in 3D and 2D. Comparisons between the model geometries are made along with a grid-sensitivity study to ensure calculation accuracy. Model verification is discussed in comparison with modeling and experimental results available in the literature.

## 2. Model description

A brief outline of the two-phase columnar solidification model is given here; additional model details can be found in a previous publication [26]. Conservation equations, sources and exchange terms, and auxiliary equations are summarized in Table 1. The main assumptions of the model include:

- The two phases in the model are the liquid melt and the solid columnar dendrite trunks.
- The morphology of the columnar dendrite trunks is approximated by step-wise growing cylinders positioned in a staggered arrangement with constant primary dendritic arm spacing,  $\lambda_1$ .
- The columnar trunks grow from the casting surface when constitutional undercooling is met and solidification follows the liquidus isotherm.
- The liquid-to-solid mass transfer (solidification/melting) rate,  $M_{\ell s}$ , is calculated as a function of the growth velocity of the columnar trunks,  $v_{Rc}$ , which is governed by diffusion of the solute in the interdendritic melt around each cylindrical trunk.
- Volume-averaged concentrations ( $c_\ell, c_s$ ) are calculated and macro-segregation is characterized by the mixture concentration,  $c_{\text{mix}}$ . Thermodynamic equilibrium is assumed at the liquid–solid interface, which dictates the liquid–solid interface concentrations ( $c_\ell^*, c_s^*$ ). Back diffusion in the solid is neglected ( $D_s = 0$ ). The concentration difference ( $c_\ell^* - c_\ell$ ) is the driving force for the growth of columnar trunks [21].

- A linearized binary Sn–Pb phase diagram with a constant solute redistribution coefficient  $k$  and a constant liquidus slope  $m$  is used.
- Interdendritic flow resistance in the mushy zone is calculated via a permeability law according to the Blake–Kozeny approach [27].
- Solidification shrinkage is not accounted for and thermosolutal convection is modeled with the Boussinesq approach.

The current model differs from some previous models [13–19, 23–25]. Firstly, The energy conservation is treated in two-phase form, implying that the temperatures of the solid and liquid are locally different, but an ‘infinite’ volumetric heat transfer between the two phases ( $H^* = 10^9 \text{ W m}^{-2} \text{ K}^{-1}$ ) is applied to level out the temperature difference. An alternative method to treat the energy conservation is to use a mixture form of energy equation [14,18,19]. The advantage of the two-phase form over the mixture form is that more freedoms are provided for handling the inter-phase enthalpy exchange, release of latent heat, and boundary conditions. The drawback of the two-phase form is that the calculation cost is relatively high.

Secondly, the meaning of the momentum exchange due to solidification-induced mass transfer,  $U_{\ell s}^M$ , is different from the one as defined in the literature [23,25,28], where  $U_{\ell s}^M$  was the momentum flux across the solid–interface due to the solidification-induced expansion/shrinkage (ignorable when the density difference between the liquid and solid phases is small). In the current model  $U_{\ell s}^M$  is calculated by the mass transfer rate ( $M_{\ell s}$ ) timing an interphase velocity ( $\bar{u}_{\ell-s}$ ) [29]. In the case of solidification, the interphase velocity  $\bar{u}_{\ell-s}$  is equal to  $\bar{u}_\ell$ . As schematically shown in Fig. 1, when the melt flows passing by a stationary growing columnar trunk (cylinder), a non-slip boundary condition applies at the liquid–solid interface, and far-field velocity of the melt is  $\bar{u}_\ell$  (intrinsic velocity). A flow boundary layer adjacent to the columnar trunk is developed. It is further assumed that the velocity profile in the boundary layer moves in the parallel direction to the growth of the columnar trunk. In a time interval of  $dt$ , the volume-averaged mass transfer due to solidification is  $M_{\ell s} \cdot dt$ . The corresponding momentum loss in the adjacent melt is  $M_{\ell s} \cdot dt \cdot \bar{u}_\ell$ . Therefore, the momentum transfer rate

**Table 1**  
Conservation equations, sources and exchange terms, auxiliary equation.

Conservative equations	
Mass:	$\frac{\partial}{\partial t} (f_\ell \rho_\ell) + \nabla \cdot (f_\ell \rho_\ell \bar{u}_\ell) = -M_{IS}$ $\frac{\partial}{\partial t} (f_s \rho_s) = M_{IS}$ (1)
Momentum:	$\frac{\partial}{\partial t} (f_\ell \rho_\ell \bar{u}_\ell) + \nabla \cdot (f_\ell \rho_\ell \bar{u}_\ell \otimes \bar{u}_\ell) = -f_\ell \nabla p + \nabla \cdot \bar{\tau}_\ell + f_\ell \rho_\ell \bar{g} - \bar{U}_{IS}^M - \bar{U}_{IS}^D$ where $\bar{\tau}_\ell = \mu_\ell (\nabla \cdot (f_\ell \bar{u}_\ell) + (\nabla \cdot (f_\ell \bar{u}_\ell))^T)$ (2)
Species:	$\frac{\partial}{\partial t} (f_\ell \rho_\ell c_\ell) + \nabla \cdot (f_\ell \rho_\ell \bar{u}_\ell c_\ell) = -C_{IS}^M$ $\frac{\partial}{\partial t} (f_s \rho_s c_s) = C_{IS}^M$ (3)
Enthalpy:	$\frac{\partial}{\partial t} (f_\ell \rho_\ell h_\ell) + \nabla \cdot (f_\ell \rho_\ell \bar{u}_\ell h_\ell) = \nabla \cdot (f_\ell k_\ell \nabla T_\ell) + Q_\ell^M - Q_{IS}^D$ $\frac{\partial}{\partial t} (f_s \rho_s h_s) = \nabla \cdot (f_s k_s \nabla T_s) + Q_s^M + Q_{IS}^D$ where $h_\ell = \int_{T_{ref}}^{T_\ell} c_p^l dT + h_\ell^{ref}$ and $h_s = \int_{T_{ref}}^{T_s} c_p^s dT + h_s^{ref}$ (4)
Solidification net mass transfer	$M_{IS} = v_{R_c} \cdot S_A \cdot \rho_s \cdot \Phi_{imp}$ (5)
Mass transfer:	$v_{R_c} = \frac{dR_c}{dt} = \frac{D_\ell}{R_c} \cdot \frac{(c_\ell^* - c_\ell)}{(c_\ell^* - c_s)} \cdot \ln^{-1} \left( \frac{R_f}{R_c} \right)$ (6)
Col. trunk growth velocity:	$d_c (= 2R_c) = \lambda_1 \cdot \sqrt{\frac{\sqrt{12} f_\ell}{\pi}}$ (7)
Diameter of col. trunks:	$R_f = \frac{1}{\sqrt{3}} \cdot \lambda_1$ (8)
Far field radius of col. trunks:	$S_A = \frac{2d_c \pi}{\sqrt{3} \lambda_1^2}$ (9)
Col. surface concentration:	$\Phi_{imp} = \begin{cases} 1 & d_c \leq \lambda_1 \\ 2\sqrt{3} \cdot f_\ell / (2\sqrt{3} - \pi) & d_c > \lambda_1 \end{cases}$ (10)
Growing surface impingement:	$\bar{U}_{IS}^D = \begin{cases} \bar{u}_\ell \cdot M_{IS} & \text{solidification} \\ 0.0 & \text{melting} \end{cases}$ $\bar{U}_{IS}^D = \frac{f_\ell^2 \mu_\ell}{K} \cdot (\bar{u}_\ell - \bar{u}_s) \text{ where } K = \lambda_2^2 \cdot \frac{f_\ell^2}{180(1-f_\ell)^2}$ (11)
Momentum transfer:	$C_{IS}^M = \begin{cases} k \cdot c_\ell^* \cdot M_{IS} & \text{solidification} \\ c_s \cdot M_{IS} & \text{melting} \end{cases}$ (12)
Species transfer:	$Q_{IS}^D = H^* \cdot (T_\ell - T_s)$ (13)
Enthalpy transfer and latent heat:	$Q_s^M = (\Delta h_f \cdot f_s + h_s) \cdot M_{IS}$ where $H^* = 10^9 \text{ W m}^{-2} \text{ K}^{-1}$ (13)
Auxiliary equation	$c_{mix} = (c_\ell \cdot \rho_\ell \cdot f_\ell + c_s \cdot \rho_s \cdot f_s) / (\rho_\ell \cdot f_\ell + \rho_s \cdot f_s)$ (14)

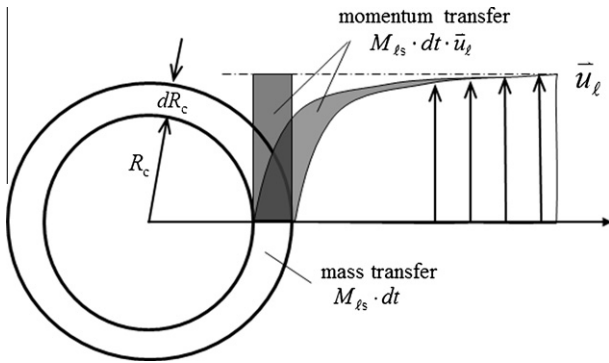


**Fig. 1.** Schematic of the velocity profile adjacent to a growing columnar trunk and momentum transfer due to solidification mass transfer.

due to phase change  $\bar{U}_{IS}^M$  is equal to  $M_{IS} \cdot dt \cdot \bar{u}_\ell$ . In the case of melting,  $\bar{u}_{\ell-s} = 0$ .

Additionally, the mass and species exchanges between the liquid and solid phases are modeled in a different way as the previous models [23,25,28]. Species balance in an ‘isolated’ volume element enveloped by a fictitious cylinder with a radius of  $R_f$  is schematically shown in Fig. 2. Each part of species transfer (due to solute partitioning at the solid–liquid interface, diffusion in the liquid region) is expressed with symbols **A** to **F**. For the simplicity of the discussion, no flow is considered, hence the species must be conserved:  $d(f_\ell \rho_\ell c_\ell + f_s \rho_s c_s) / dt = 0$ , i.e.

$$A + \rho_s c_s \frac{df_s}{dt} - B + F - \rho_\ell c_\ell^* \frac{df_\ell}{dt} + D = 0 \quad (15)$$

As  $A = B$  and  $E = D + F$ , then

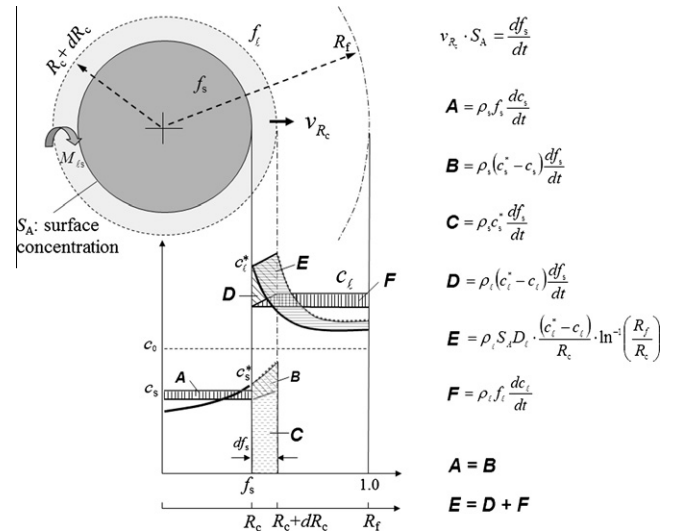


**Fig. 2.** Schematic of interfacial mass and species transfer. Species conservation is considered in an ‘isolated’ volume element enveloped by a fictitious cylinder with a radius of  $R_f$ .

$$E = \rho_\ell (c_\ell^* - c_s) \frac{df_s}{dt} \quad (16)$$

Replace **E** and  $\frac{df_\ell}{dt}$  in Eq. (16) with the expressions in Fig. 2, we have

$$\rho_\ell S_A D_\ell \frac{(c_\ell^* - c_\ell)}{R_c} \ln^{-1} \left( \frac{R_f}{R_c} \right) = \rho_\ell (c_\ell^* - c_s) \cdot v_{R_c} \cdot S_A \quad (17)$$

The formulations for the columnar trunk growth velocity (Eq. (6)) and the solidification net mass transfer rate (Eq. (5)) are obtained.

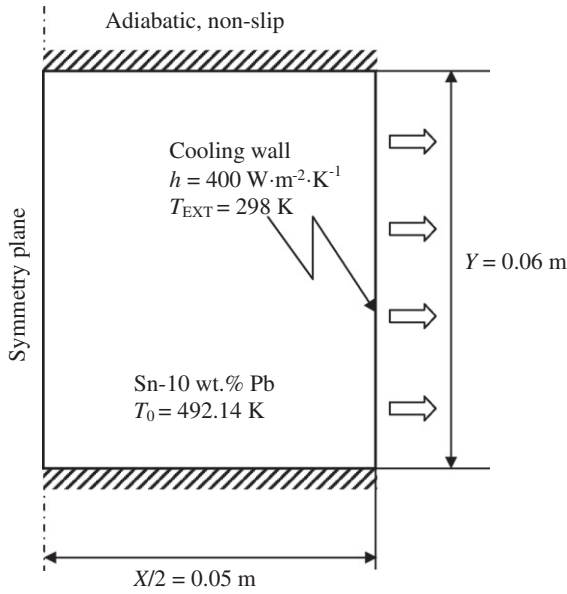


Fig. 3. Benchmark geometry with boundary and initial conditions.

It is clear that the growth of the columnar trunk is governed by diffusion of species around the growing columnar trunk. This diffusion happens only in the melt region.

The interfacial net species transfer due to solidification is:  $C_{is}^M = M_{is} \cdot c_s^*$ . No additional diffusive species transfer is necessarily considered, as there is no net species flux across the liquid–solid interface without solidification. For remelting, the interfacial net species transfer is modeled according to Beckermann and co-author [25]:  $C_{is}^M = M_{is} \cdot c_s$ .

The conservation equations in Table 1 are numerically solved using FLUENT<sup>®</sup> 6.3.26 [29], which uses a control-volume finite difference numerical method. All phases share a single pressure field,  $p$ , which is solved via a pressure correction equation obtained from the sum of the normalized mass continuity equations using the phase coupled SIMPLE (PC-SIMPLE) algorithm.

Table 2  
Thermo-physical properties and model parameters.

Property	Symbol	Units	Quantity
Nominal concentration	$c_0$	wt.% Pb	10.0
Melting point at $c = 0$	$T_m$	K	505
Eutectic composition	$c_e$	wt.% Pb	38.1
Eutectic temperature	$T_e$	K	456
Liquidus slope	$m$	K (wt.%) <sup>-1</sup>	-1.286
Equilibrium partition coefficient	$k$	-	0.0656
Reference density	$\rho_{ref}$	kg m <sup>3</sup>	7000
Specific heat	$c_p^l, c_p^s$	J kg <sup>-1</sup> K <sup>-1</sup>	260
Thermal conductivity	$k_l, k_s$	W m <sup>-1</sup> K <sup>-1</sup>	55.0
Latent heat	$\Delta h_f$	J kg <sup>-1</sup>	$6.1 \times 10^4$
Viscosity	$\mu_l$	Kg m <sup>-1</sup> s <sup>-1</sup>	$1.0 \times 10^{-3}$
Liquid thermal expansion coefficient	$\beta_T$	K <sup>-1</sup>	$6.0 \times 10^{-5}$
Liquid solutal expansion coefficient	$\beta_C$	wt.% <sup>-1</sup>	$-5.3 \times 10^{-3}$
Primary dendritic arm spacing	$\lambda_1$	m	$1.3 \times 10^{-3}$
Second dendritic arm spacing <sup>a</sup>	$\lambda_2$	M	3.25 (or $4.55 \times 10^{-4}$ )
Diffusion coefficient (liquid)	$D_l$	m <sup>2</sup> s <sup>-1</sup>	$1.0 \times 10^{-8}$
Initial temperature	$T_0$	K	492.14
Heat transfer coefficient	$h$	W m <sup>-2</sup> K <sup>-1</sup>	400
External temperature	$T_{EXT}$	K	298
Dimension of the 2D cavity	$X \times Y$	m	$0.1 \times 0.06$
Grid size <sup>a</sup>		m	$0.25$ (or 0.5, 1, $2 \times 10^{-3}$ )

<sup>a</sup> Parameters varied in parameter study.

For each time-step, up to 60 iterations are necessary to reach solution convergence as determined by a decrease of the normalized residuals of  $f_\ell$  and  $\bar{u}_\ell$  below  $10^{-4}$ , of  $c_\ell$  and  $c_s$  below  $10^{-5}$ , and of  $h_\ell$  and  $h_s$  below  $10^{-7}$ . Choice of a time step that ensures a high accuracy solution must be determined empirically by test simulations. In this study all calculations are run with a time-step of 0.0005 s. All simulations are run in parallel on 8 CPUs (Intel Nehalem Cluster 2.93 GHz), with simulation times close to 3 months for the 3D case and 7–15 days for the 2D cases, depending on mesh size.

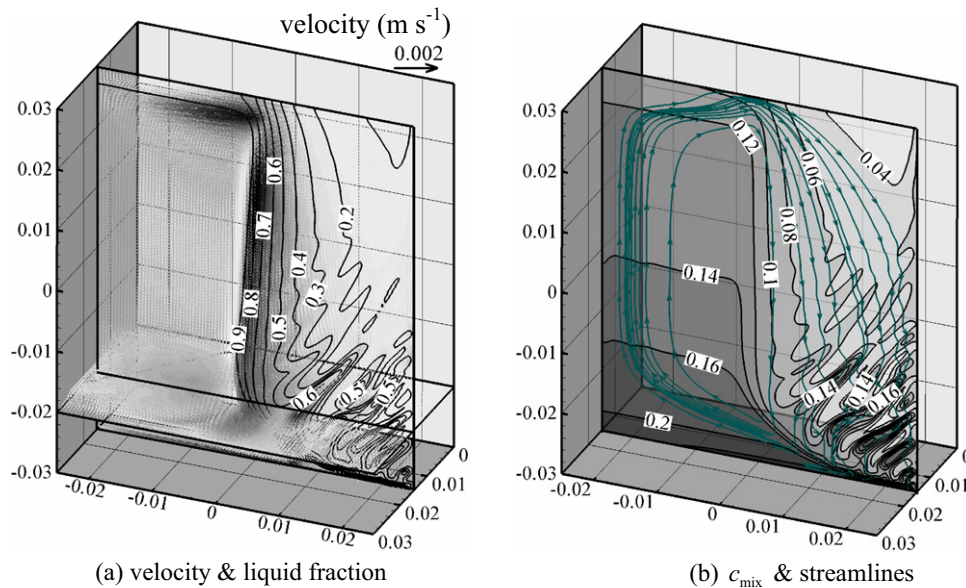
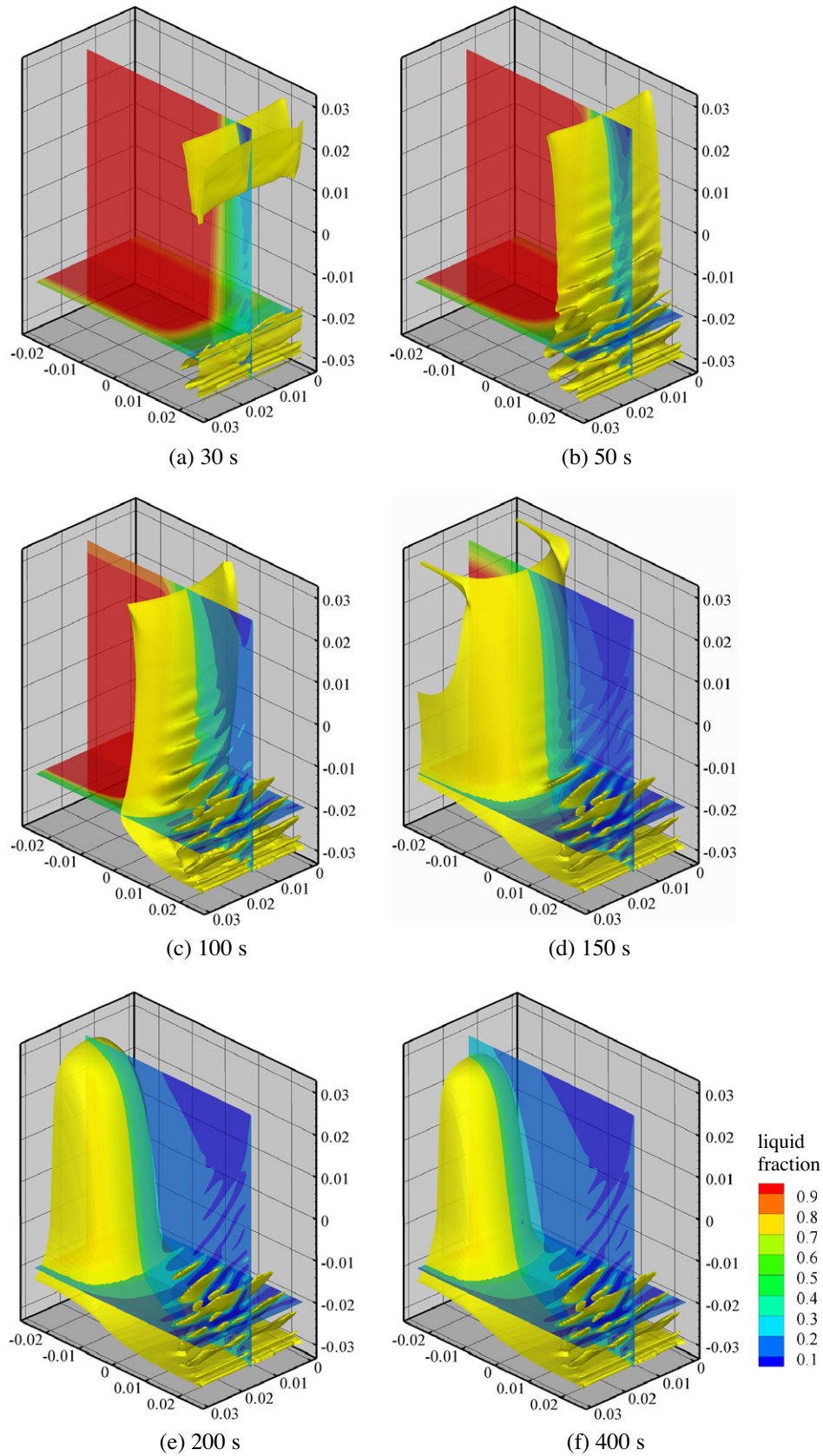
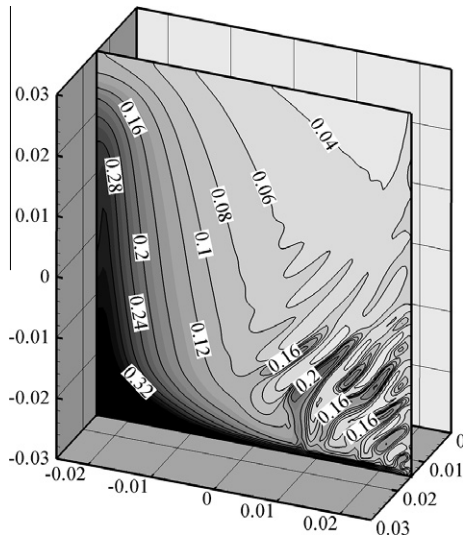


Fig. 4. Transient 3D simulation results at 100 s are shown: (a) velocity vectors in two planes (a vertical plane and a horizontal plane 0.01 m from bottom) and liquid volume fraction isolines with labeled values in the vertical center plane; (b) in the vertical plane,  $c_{mix}$  in gray scale (dark for the highest and light for the lowest value),  $c_{mix}$  isolines labeled with corresponding values, and streamlines of the melt flow.



**Fig. 5.** Evolution of solidification in the 3D benchmark with 0.03 m thickness at (a) 30 s, (b) 50 s, (c) 100 s, (d) 150 s, (e) 200 s, and (f) 400 s. The liquid volume fraction in two planes (a vertical center plane and a horizontal plane with 0.01 m from bottom) is shown in color scale. The isosurfaces (yellow) of liquid volume fraction ( $f_l = 0.35$ ) are also shown to demonstrate the evolution of the flow channels.



**Fig. 6.** Distribution of the Pb mixture concentration,  $c_{\text{mix}}$ , at the end of solidification is shown in gray scale (dark for the highest and light for the lowest value) along with labeled  $c_{\text{mix}}$  isolines.

### 3. Benchmark configuration

Benchmark simulations are carried out for one 2D and two 3D configurations. A sketch of the 2D benchmark configuration described by Bellet et al. [1] is shown in Fig. 3, labeled with boundary and initial conditions. Due to the geometric and heat extraction symmetry of the Bellet ingot, half of the ingot is modeled and a symmetry boundary condition is defined at the left boundary. The 3D geometries have the same cross-sectional dimensions as shown in Fig. 1 with a thickness of 0.03 in one case and 0.05 in the second case. The casting alloy is Sn–10 wt.% Pb. In the 2D model heat is extracted from one vertical wall and a symmetry boundary condition is imposed at the centerline. At time  $t = 0$ , the mold is filled with melt at uniform temperature and composition. The mold walls have a constant temperature,  $T_{\text{EXT}}$ , and a constant heat transfer coefficient,  $h$ , is applied between the casting and the mold. The 3D simulations have the same boundary conditions as the 2D case with non-slip front and back walls treated with a convective cooling boundary condition where  $h = 50 \text{ W m}^{-2} \text{ K}^{-1}$  and  $T_{\text{EXT}} =$

298 K. The calculation was run to the end of solidification at ca. 490 s. Thermo-physical properties, boundary conditions and numerical parameters are given in Table 2.

## 4. Simulation results

### 4.1. Evolution of 3D channels

Transient simulation results for the 3D benchmark with 0.03 m thickness at 100 s are shown in Fig. 4. In Fig. 4a, melt velocity vectors are shown in two planes (a vertical plane and a horizontal plane with a distance of 0.01 m from the bottom) and liquid volume fraction isolines are shown in the vertical plane. In Fig. 4b,  $c_{\text{mix}}$  isolines, flow streamlines, and the Pb solute mixture concentration,  $c_{\text{mix}}$ , are shown.

As seen in Fig. 4a, when the liquid fraction is larger than 0.4, the flow is relatively strong while in the region where the liquid fraction is less than 0.3 velocities are negligible, less than  $0.0003 \text{ m s}^{-1}$ . The low velocity regions correlate with the dendritic mushy zone where the liquid fraction is smaller than 0.3. For the alloy Sn–10 wt.% Pb, the interdendritic melt, enriched with Pb, has a higher density than the bulk melt, and both the thermal and solute buoyancy forces lead to a downward flow along the solidification front. This forms a large clockwise circulation in the domain, as the streamlines in Fig. 4b show. In the right bottom region of the vertical plane, the flow channels which have formed can be seen. As the channels form, the flow (streamlines) is significantly diverted. This diversion is a result of the relatively higher volume fraction of liquid (and thus higher permeability) within a channel in comparison to the channel-wall region. The interdendritic melt will preferentially take its path along the channel, and the streamlines are periodically diverted from one channel, through the channel walls, to the neighboring channels.

Fig. 5a–f show snapshots of the evolution of solidification at  $t = 30, 50, 100, 150, 200$  and  $400$  s for the 3D benchmark with 0.03 m thickness. In each frame the liquid fraction distributions are shown in a vertical center plane and horizontal plane as in Fig. 4a. Isosurfaces (yellow) of liquid volume fraction ( $f_l = 0.35$ ) are also shown to demonstrate the evolution of the flow channels. The regions bounded by the isosurfaces, where  $f_l$  is larger than 0.35, represent the flow channels. At 30 s the channels have formed in the right bottom region adjacent to the chill wall, but they are not well pronounced. At 50 s, the number of channels near the chilled wall

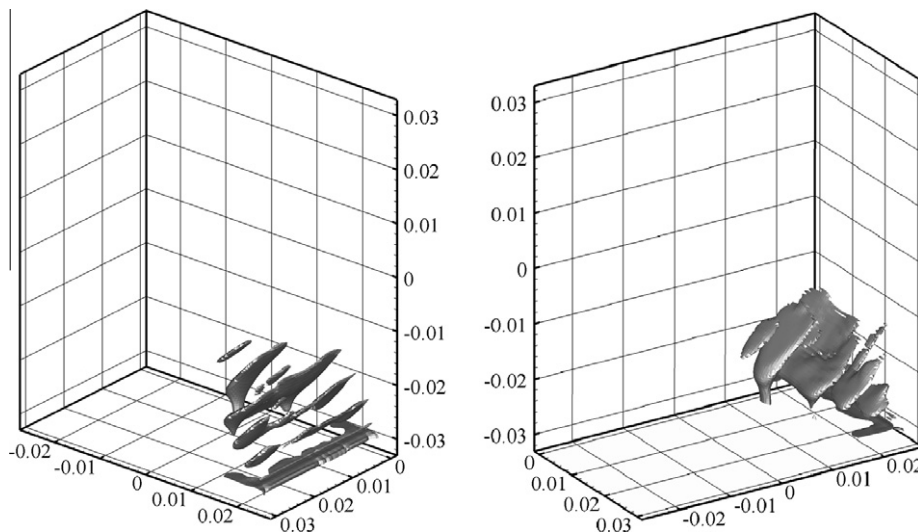


**Fig. 7.** The isosurface of Pb segregation ratio, as defined by  $(c_{\text{mix}} - c_0)/c_0 = 1.5$  from two viewing angles.

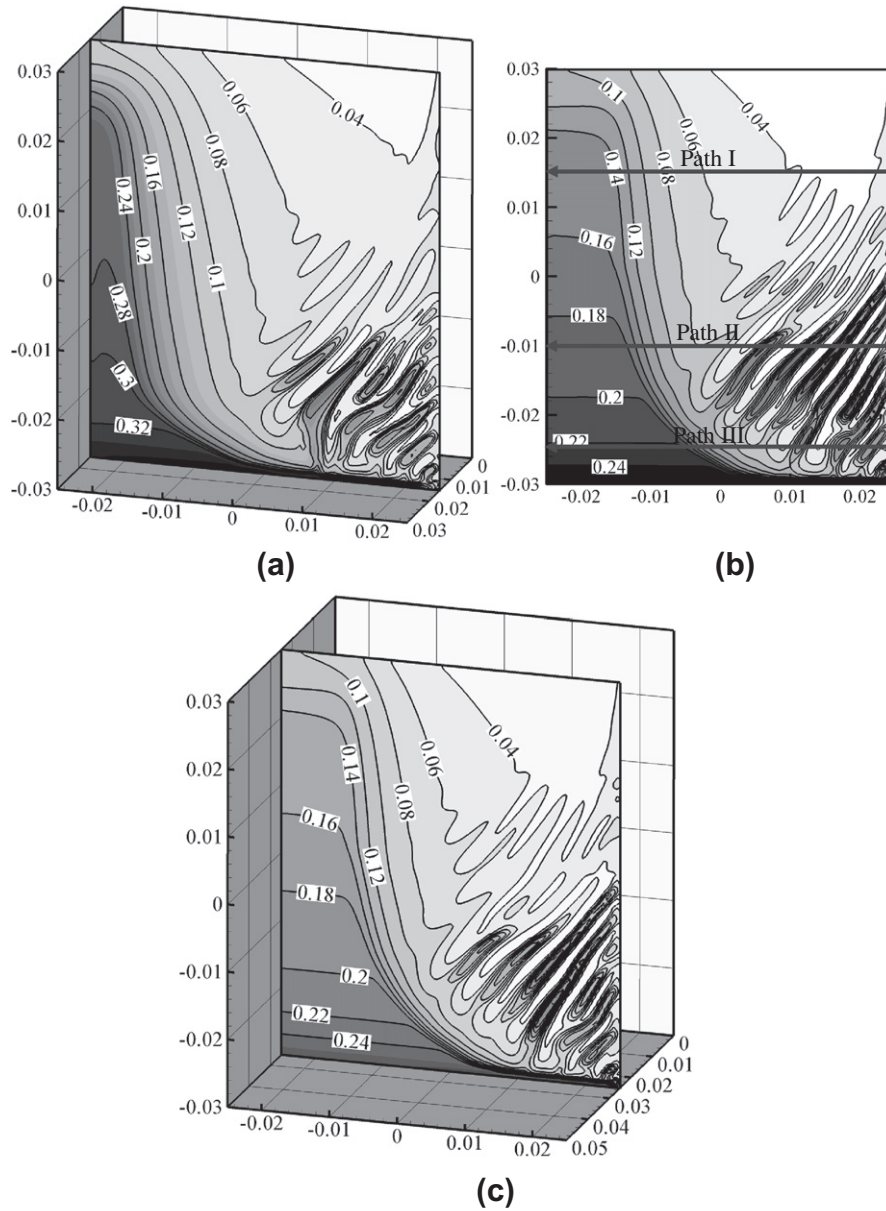


**Fig. 8.** Comparison of  $c_{mix}$  at  $t = 200$  s for (a) center plane of 3D benchmark with thickness of 0.03 m; (b) 2D benchmark; and (c) center plane of 3D benchmark with thickness of 0.05 m.  $c_{mix}$  is shown in gray scale (dark for the highest and light for the lowest value) with labeled  $c_{mix}$  isolines.

region has grown and a portion of these are already fully developed. After 200 s the channels become relatively stable and fixed, with very little additional growth. The channels are generally 3D in nature, most of them are lamellar-structured, discontinuous, while a few of them are rod-like. They occur only in the right bottom region, which is roughly a quarter of the whole calculation domain. The channel spacing (distance between neighboring channels) is nearly constant, varying slightly over time during solidification.

The sequence of global solidification snapshots in Fig. 5 show that in the upper part of the ingot the solidification front, approximated with the isosurface of  $f_l = 0.35$ , sweeps across the domain much faster than in the bottom region. This is caused by the downward flow in the mushy zone, which transports the Pb-rich interdendritic melt from the upper to the lower region; hence the liquidus temperature decreases in the lower region. As a consequence, the solidification rate in the lower region is retarded.

The macrosegregation profile of the solidified ingot in the vertical center plane is shown in Fig. 6. Negative segregation, with

$c_{mix}$  as small as 0.04, is predicted in the upper-right region and positive segregation, with  $c_{mix}$  as large as 0.32, is predicted in the lower-left region. The channel segregation pattern is clearly shown in the lower right region. The pattern of the segregates (inclined angle, channel spacing, number of the channels) corresponds to the flow patterns that develop during solidification (Fig. 5).

Fig. 7 shows the final channel segregation pattern in 3D from two angles. The isosurface of segregation ratio, as defined by  $(c_{mix} - c_0)/c_0 = 1.5$ , is displayed. The channel segregates are predominately lamellar-structured with some rod-like morphology, which is in agreement with 3D channel segregation previously described in the literature [6,7]. In the current benchmark, the channel segregation pattern is observed only in the lower right region and shows an upward slanting pattern with an angle of 40–60° from the horizontal plane. The average thickness of the channels is 0.002 m, the channel spacing is 0.004 m and the length of the largest channel is approximately 0.019 m.

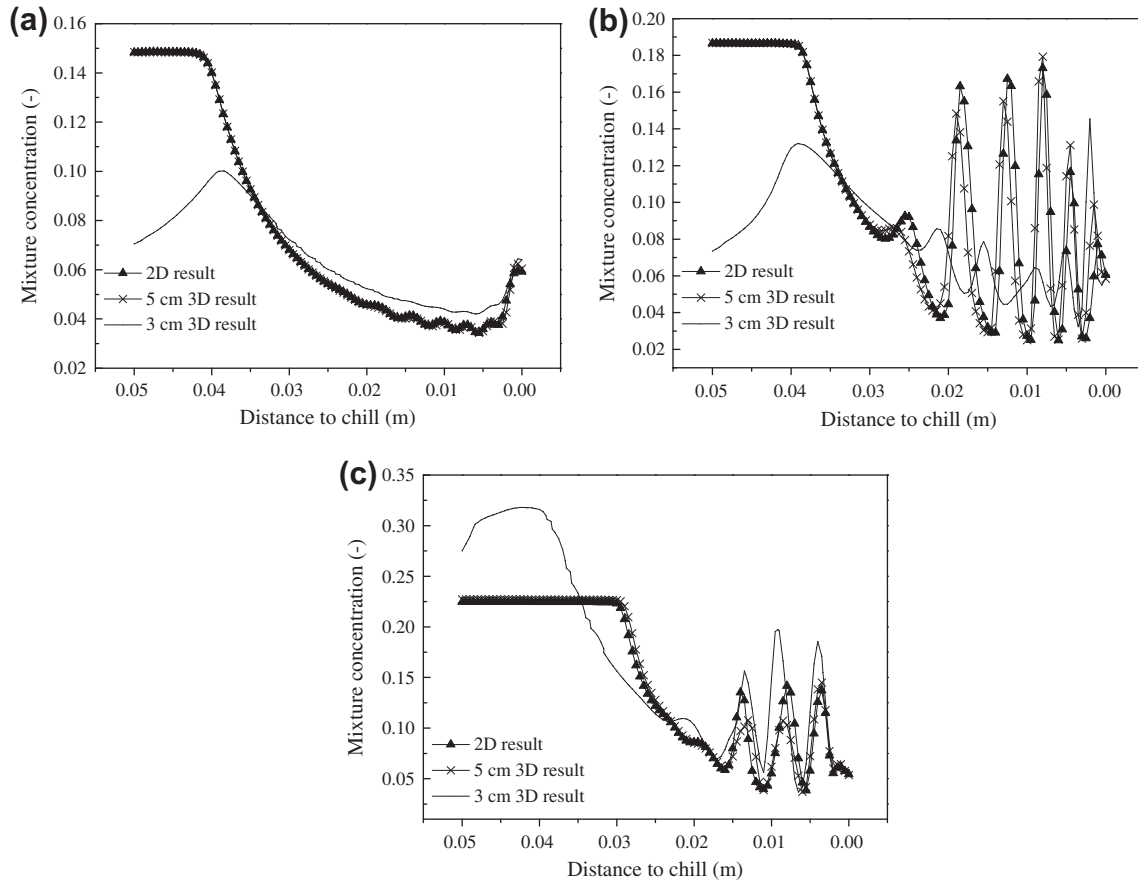


**Fig. 9.** Comparison of  $c_{\text{mix}}$  distributions of the 2D and 3D cases along paths I to III as marked in Fig. 8(b). (a) Path I, on the center plane, 0.045 m from the bottom; (b) Path II, in the center plane, 0.02 m from the bottom; (c) Path III, in the center plane, 0.005 m from the bottom.

#### 4.2. Comparison of 3D and 2D calculations

Transient results at 200 s for the 3D and 2D benchmark cases are compared in Fig. 8. Fig. 8a shows the  $c_{\text{mix}}$  distribution in the center plane of the 3D benchmark with 0.03 m thickness and Fig. 8b presents the corresponding 2D  $c_{\text{mix}}$  distribution. The 3D and 2D calculations predict similar channel segregation patterns, however, the severity of the macrosegregation of these two cases is significantly different. For example, the maximum Pb concentration in the lower left region of the 3D benchmark is 0.32, much higher than the maximum Pb concentration of 0.24 in the same region of the 2D case. This difference is called the 3D effect. The front and back walls of the 3D benchmark with finite thickness of 0.03 m have significant influence on the internal flow intensity, hence on the transport of segregated solute elements. To show the diminishing 3D effect as casting thickness increases, a corresponding 3D benchmark with a thickness of 0.05 m was simulated, and is shown in Fig. 8c. It is found that with a casting thickness of 0.05 m the  $c_{\text{mix}}$  distribution in the center plane (Fig. 8c) is almost identical to the 2D result (Fig. 8b), with respect to both the channel segregation pattern and the severity of the macrosegregation. Fig. 9 compares the 2D and 3D  $c_{\text{mix}}$  distribution profiles along three paths as marked in Fig. 8b. The difference in distribution between the 2D and the 3D with thickness of 0.03 m is significant. However, the difference between the 2D and the 3D with thickness of 0.05 m is minor. The 3D effect decreases for the benchmark with larger thickness, i.e. the segregation pattern on the center plane of the 3D case can be reproduced by a 2D calculation. Based on this conclusion, the analysis and discussion in the following sections are based on 2D simulations.

## 5. Verifications

### 5.1. Grid sensitivity

A grid study was carried out on four grids with cell sizes of 0.25, 0.5, 1 and 2 mm respectively. For this study the secondary dendrite arm spacing ( $3.25 \times 10^{-4}$  m) and other physical and process parameters are kept constant. Fig. 10 shows the liquid fraction and Fig. 11 the Pb solute mixture concentration,  $c_{\text{mix}}$ , at 200 s for each grid size. The temperature isotherms are nearly identical for all cases, thus the grid with 2 mm cell size is fine enough to resolve the temperature field. The liquid volume fraction and segregation patterns are more sensitive to cell size, especially in the lower right corner region where the channel segregates appear. Firstly, the coarse grid calculation has only one to two channels close to the lower right corner, while the fine grid calculation has more channels in a broader region near the lower right corner. The trend shows that simulations with finer grids predict more channels. Additionally, as cell size decreases the size of the channel and the channel spacing (distance between the neighboring channels) become smaller and the length of the channels becomes longer.

When the cell size is smaller than 0.5 mm, the difference in segregation pattern from case to case is not as great as cases with grid size larger than 0.5 mm – a significant finding of the current study. To further quantify the influence of grid size on the segregation pattern, the estimated average channel length and channel spacing as a function of mesh size are compared in Fig. 12. The channel spacing decreases with grid refinement, while the average length of the channel increases. It is noted that there is only a slight difference in channel size between the 0.5 mm grid and 0.25 mm grid.

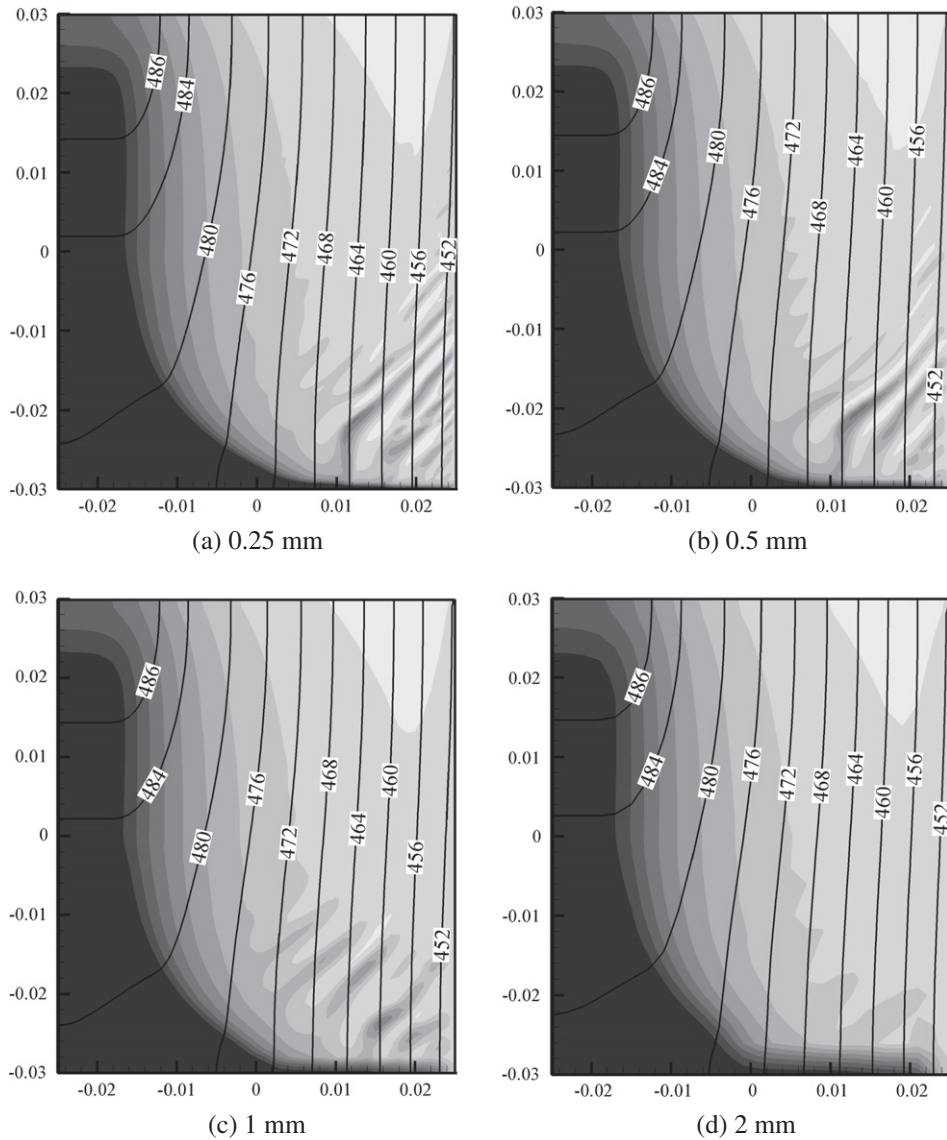


**Fig. 10.** Grid sensitivity of the temperature field and volume fraction of liquid at 200 s. The volume fraction of liquid is shown in gray scale (dark for the highest and light for the lowest value), overlaid with isotherms of the temperature [K] for (a) grid size is 0.25 mm; (b) 0.5 mm; (c) 1 mm; and (d) 2 mm.

The average channel length appears to be approaching a constant of 20.5  $\mu\text{m}$ , and the average channel spacing is approaching a constant of 6  $\mu\text{m}$ .

Fig. 13 shows the influence of mesh size on the  $c_{\text{mix}}$  distribution profile along the Path IV as marked in Fig. 11a. The  $c_{\text{mix}}$  curves for each grid coincide in the no-channel region, i.e. at 0.025 m or further from the chilled surface. In the region with channel segregates, close to the chilled surface, the  $c_{\text{mix}}$  curves differ, particularly when the grid size is larger than 0.5 mm. However, the difference between the  $c_{\text{mix}}$  curves of the fine grids (e.g. 0.25 and 0.5 mm) is quite small. According to Kumar et al [14], the grid should be fine enough to resolve the flow through the channel, i.e. at least three grid points (volume elements) should be located in each channel. As shown in Fig. 13, there are 6 grid points in each channel for the case of grid resolution of 0.5 mm, and 12 grid points in each channel for the case of grid resolution of 0.25 mm.

Based on the above findings, it is anticipated that a quasi grid-independent result is reached with a grid size of 0.5 mm for the current benchmark. The characteristic parameters (average channel spacing, length and the severity of the segregation) will

approach constant values, however the fine details of the  $c_{\text{mix}}$  distribution contours will change slightly with further refinement of the grid size.

## 5.2. Comparison with other numerical modeling results

A simulation using the current finite volume numerical model with a 2D ( $0.1 \times 0.06 \text{ m}^2$ ) benchmark geometry with alloy Sn–5 wt.% Pb is compared to the same benchmark studied by Ahmad et al. [17] with a finite element model and by Roux et al. [30] with a chemical non-equilibrium model. In this benchmark, heat is extracted from the left vertical wall with a heat transfer coefficient of  $300 \text{ W m}^{-2} \text{ K}^{-1}$ . At  $t = 0$  the domain is filled with a liquid binary metal at a uniform temperature and composition. A detailed model description, material properties and process parameters can be found in Refs. [17,30]. Fig. 14 shows a comparison of the  $c_{\text{mix}}$  distribution for the current model, the non-equilibrium model [30] and the FEM model [17], at 400 s of solidification. The current model (Fig. 14a) is in very good agreement with the non-equilibrium model (Fig. 14b), and shows reasonable agreement with the

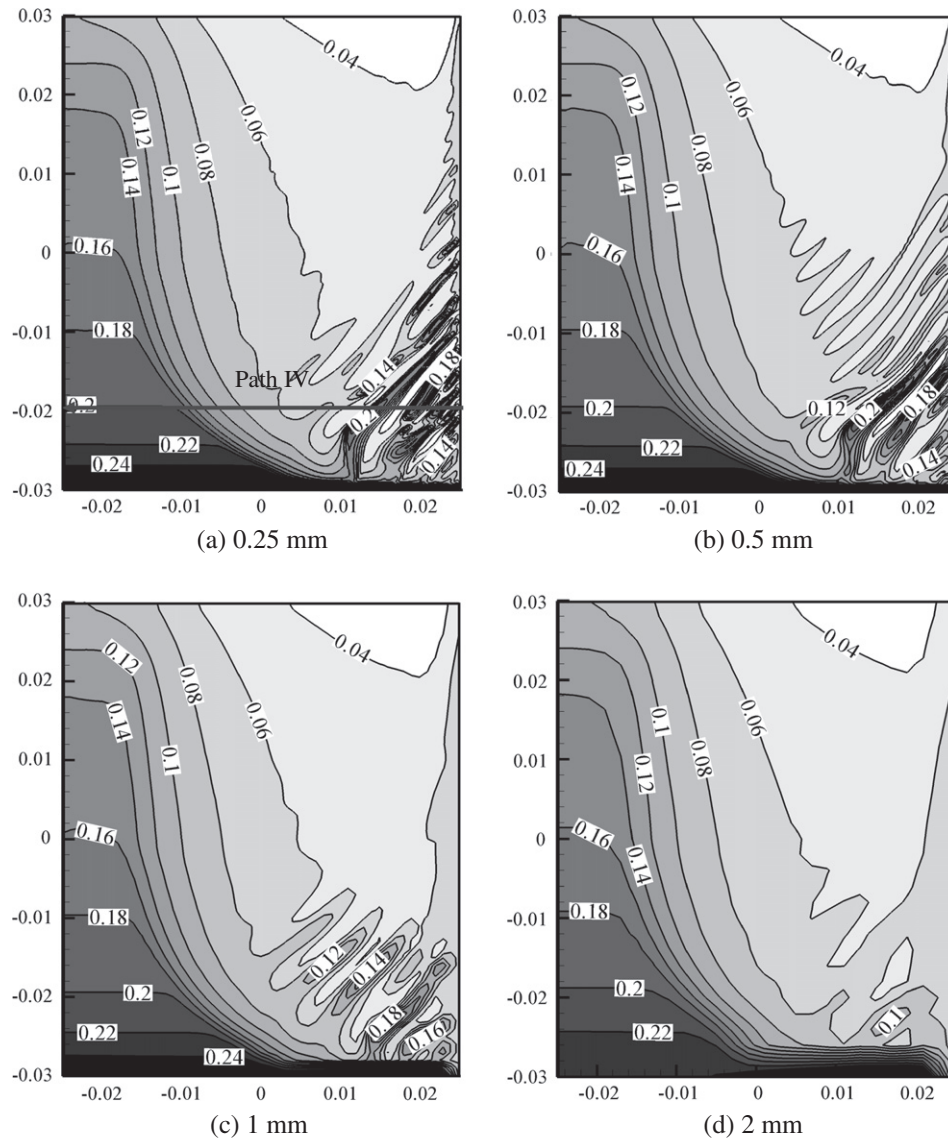


**Fig. 11.** Grid sensitivity of macrosegregation at 200 s. The Pb mixture concentration,  $c_{\text{mix}}$ , is shown in gray scale with dark for the highest and light for the lowest value and overlaid with  $c_{\text{mix}}$  isolines for grid size of (a) 0.25 mm; (b) 0.5 mm; (c) 1 mm; and (d) 2 mm.

FEM model (Fig. 14c). All three models predict a high solute enrichment with a strong concentration gradient in the lower right of the domain.

### 5.3. Experimental verification

The current model is also evaluated by comparing the modeling results with the results of Hebditch and Hunt [20], as shown in Fig. 15. The variation of relative Pb average mass fraction (displayed as percentage of the mean composition) are plotted as a function of the distance to the cooling wall along four paths, namely 0.005 m, 0.025 m, 0.045 m and 0.055 m from the bottom. Agreement is fairly good, especially in the upper part of the cavity along the paths of 0.045 m and 0.055 m, where negative segregation is observed. The Pb mass fraction differs near the bottom of the cavity (0.005 m), where a strong positive segregation is observed at the end of the solidification. The Pb composition from the experiment is higher than the predicted result from the simulation, however this is to be expected since the simulation is 2D while the experimental geometry is of course 3 dimensional with a very thin thickness (0.013 m). The experimental result has strong

3D effects, so the value of the composition should be higher than the corresponding 2D results. Recalling the comparison of 2D and 3D simulation results in Fig. 8, the predicted maximum positive

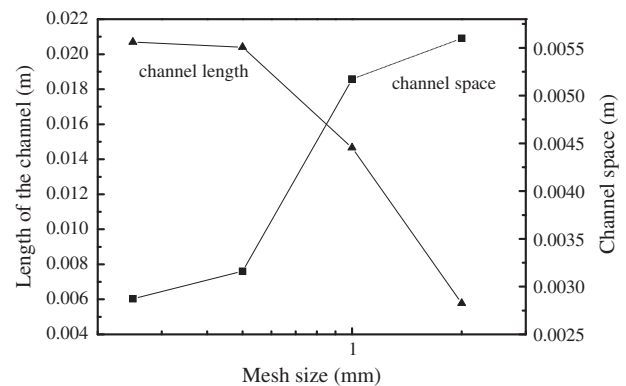


**Fig. 12.** The predicted average length and spacing of channels as function of the mesh size.

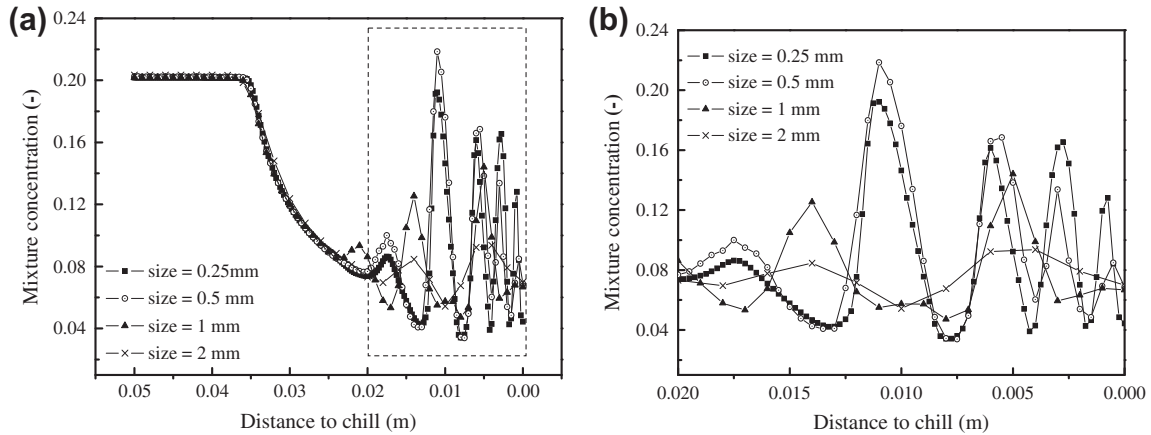


Fig. 13. Influence of the mesh size on the  $c_{mix}$  distribution profile along the path IV as marked in Fig. 11(a); (b) zoomed-in view of the right part region of (a).

segregation in the low corner last-to-solidify region is significantly higher for the 3D case. The 3D effect is significant for the 3D experimental benchmark with a 0.013 m thickness.

### 6. Discussion

A two-phase columnar solidification model was used to simulate the formation of channel segregates and expand the understanding of the mechanisms that lead to channel segregation. Solidification of a reference Sn–Pb benchmark, as defined by Bellet et al. [1], was calculated. The main findings are as follows.

1. The 3D simulations show the transient development of the channel segregation. In the current alloy system the thermo-solutal buoyancy drives the clockwise circulation flow, i.e. the segregated interdendritic melt is heavier than the bulk melt and sinks downward along the solidification front. Channel segregates form in the bottom corner near the chilled wall with a predominately discontinuous lamellar-structured morphology and some rod-like formation.
2. Significant differences in  $c_{mix}$  distribution are observed between the 2D calculation and the center plane of the 3D calculation with 0.03 m thickness. This difference, the 3D effect, is caused by the thermal and hydrodynamic influence of the front/back mold walls. The 3D effect is much less prominent in the thicker benchmark ( $\geq 0.05$  m), thus the 2D calculation suitably represents the thick-walled ( $\geq 0.05$  m) 3D benchmark but not the thinner 3D benchmark. As a corollary, caution must be used when comparing 2D modeling results with 3D experiments. Despite this, the efficient computation time of a 2D simulation makes them a worthy analysis tool.
3. To ensure calculation accuracy, the influence of grid size on channel segregation formation was evaluated. In the current benchmark, a quasi grid-independent result can be achieved with a cell size less than 0.5 mm. This quasi grid-independence means that the characteristic parameters (average channel spacing, length and severity of the segregation) tend to converge to constant values, although the fine features of the  $c_{mix}$  contours change slightly with further refinement of the grid. The current mesh resolution (0.25 mm) may not be fine enough to produce grid-converged result of the fine channel segregates details, but the most important features regarding the formation of channel segregates can be resolved with the current mesh resolution. This finding coincides with the statement of Kumar et al [14].
4. Verification of the current model was made by comparison with other modeling approaches [17,30] and with the experiments of Hebditch and Hunt [20]. General quantitative agreements were

obtained, however, these models and experiments have not been able to describe details of the channel segregates in 3D. A more detailed comparison of the current model is possible with the experimental work by Sawada et al. [18] who presented a stereoscopic structure of the channel segregates with X-ray CT method on a Sn–20 wt.%Bi benchmark ( $0.1 \times 0.11 \times 0.03$  m<sup>3</sup>). In this experiment, the channels were more rod-like than lamellar. In the current modeling result, mostly lamellar structure is observed. This discrepancy may arise from (1) differences in alloy system, benchmark geometry and boundary

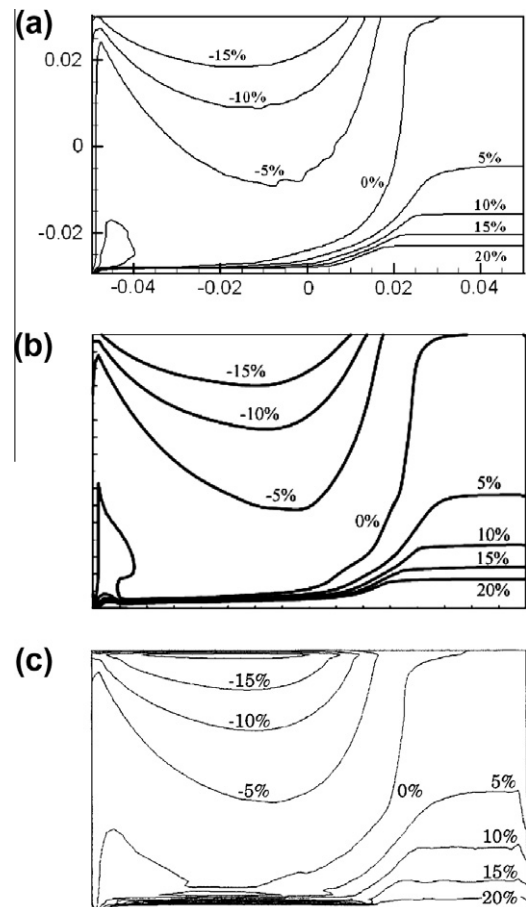
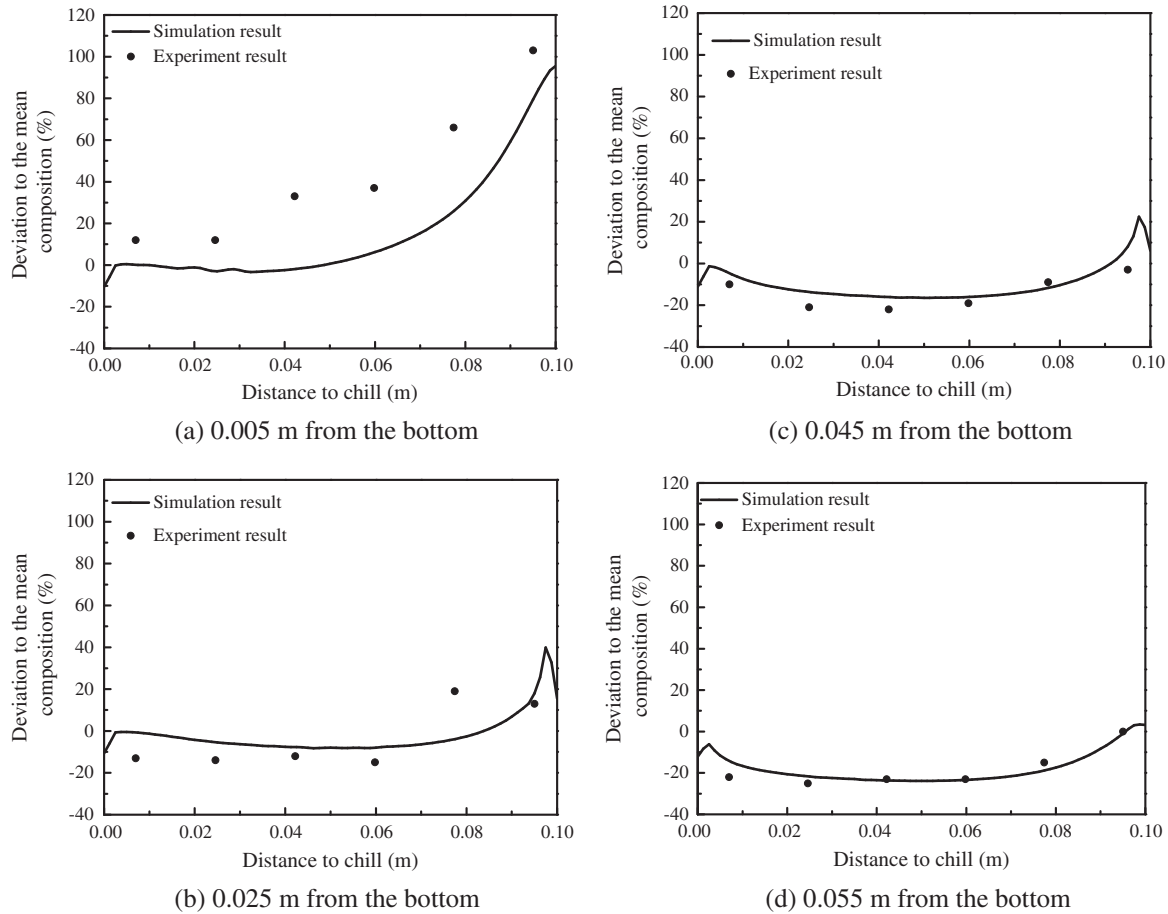


Fig. 14. Predicted segregation patterns in the Sn–5 wt.% Pb benchmark at 400 s: (a) the current model; (b) chemical non-equilibrium model in [30] and (c) FEM model in [17].



**Fig. 15.** Relative Pb mass fraction variations,  $((c_{\text{mix}} - c_0)/c_0) \times 100$ , for the Sn–5 wt.% Pb benchmark at the end of solidification as a function of the distance from the cooling wall. These profiles correspond to four heights of the cavity at (a) 0.005 m; (b) 0.025 m; (c) 0.045 m; and (d) 0.055 m from the bottom.

conditions or (2) from the uncertainties of model assumptions and model parameters, such as the assumption of the isotropic permeability of the mushy zone, the limitation of the volume average technique, etc. To clarify this issue, further experiments are planned in collaboration with Frautrelle [31] based on the same Sn–Pb benchmark.

Part II of this investigation presents an in-depth discussion and parameter study on the formation mechanisms of channel segregation.

## Acknowledgments

The authors would like to thank Prof. H. Combeau from CNRS-Nancy and Prof. Y. Frautrelle from CNRS-SIMAP-EPM, France for contributing discussions on the current modeling results. Financial support for this project is provided by the Austrian Federal Ministry of Economy, Family and Youth and the National Foundation for Research, Technology and Development. Author Jun Li would like to thank the China Scholarship Council for financial support.

## References

- [1] M. Bellet, H. Combeau, Y. Fautrelle, D. Gobin, M. Rady, E. Arquis, O. Budenkova, B. Dussoubs, Y. Duterrail, A. Kumar, C.A. Gandin, B. Goyeau, S. Mosbah, M. Založnik, *Int. J. Therm. Sci.* 48 (2009) 2013–2016.
- [2] K. Suzuki, T. Miyamoto, *Trans. ISIJ* 18 (1978) 80–89.
- [3] J.A. Van Den Avyle, J.A. Brooks, A.C. Powell, *JOM* 50 (1998) 22–25.
- [4] K. Suzuki, K. Taniguchi, *Trans. Iron Steel Inst. Jpn.* 21 (1981) 235–242.
- [5] K. Suzuki, T. Miyamoto, *Trans. Iron Steel Inst. Jpn.* 20 (1980) 375–383.
- [6] J.J. Moore, N.A. Shah, *Int. Metals Rev.* 28 (1983) 338–356.
- [7] E. Marburg, *Trans. AIME* 5 (1953) 157–172.
- [8] S.N. Tewari, R. Shah, *Metall. Trans. A* 23A (1992) 3383–3392.
- [9] M.I. Bergman, D.R. Fearn, J. Bloxham, M.C. Shannon, *Metall. Mater. Trans. A* 28A (1997) 859–866.
- [10] R.J. McDonald, J.D. Hunt, *Trans. Metall. Soc. AIME* 245 (1969) 1993–1997.
- [11] R.J. McDonald, J.D. Hunt, *Metall. Trans.* 1 (1970) 1787–1788.
- [12] J.R. Sarazin, A. Hellawell, *Metall. Trans. A* 19A (1988) 1861–1871.
- [13] G. Quillet, A. Ciobanas, P. Lehmann, Y. Fautrelle, *Int. Sci. Colloquium Modelling for Electromagnetic Processing Hannover March 24–26, 2003*, pp. 171–176.
- [14] A. Kumar, B. Dussoubs, M. Založnik, H. Combeau, *J. Phys. D: Appl. Phys.* 42 (2009) 105503–105515.
- [15] H. Shahani, G. Amberg, H. Fredriksson, *Metall. Trans. A* 23A (1992) 2301–2311.
- [16] M.C. Schneider, C. Beckermann, *Int. J. Heat Mass Transfer* 38 (1995) 3455–3473.
- [17] N. Ahmad, H. Combeau, J. Desbiolles, T. Jaldanti, G. Lesoult, J. Rappaz, M. Rappaz, C. Stomp, *Metall. Mater. Trans. A* 29A (1998) 617–630.
- [18] T. Sawada, K. Oikawa, K. Anzai, in: S.L. Cockcroft, D.M. Maijer (Eds.), *Modeling of Casting, Welding and Advanced Solidification Processes*, vol. XII, TMS, Warrendale, PA, USA, 2009, pp. 303–309.
- [19] M. Založnik, H. Combeau, in: S.L. Cockcroft, D.M. Maijer (Eds.), *Modeling of Casting, Welding and Advanced Solidification Processes*, vol. XII, TMS, Warrendale, PA, USA, 2009, pp. 253–260.
- [20] D.J. Hebditch, J.D. Hunt, *Metall. Trans.* 5 (1974) 1557–1564.
- [21] M. Wu, A. Ludwig, *Metall. Mater. Trans. A* 37A (2006) 1431–1613.
- [22] M. Wu, A. Ludwig, *Metall. Mater. Trans. A* 38A (2007) 1465–1475.
- [23] J. Ni, C. Beckermann, *Metall. Trans. B* 22B (1991) 349–361.
- [24] C.Y. Wang, C. Beckermann, *Metall. Mater. Trans. A* 27A (1996) 2754–2764.
- [25] C. Beckermann, R. Viskanta, *Appl. Mech. Rev.* 46 (1993) 1–27.
- [26] A. Ludwig, M. Grasser, M. Wu, A. Kuhn, J. Riedle, *Int. J. Fluid Dyn. Mater. Proc.* 1 (2006) 285–300.
- [27] R.B. Bird, W.E. Stewart, E.N. Lightfoot, *Transport Phenomena*, John Wiley & Sons, New York, 1960.
- [28] M. Založnik, H. Combeau, *Comput. Mater. Sci.* 48 (2010) 1–10.
- [29] *Fluent 6.3.26 User's Guide*, 2009 (Chapter 18).
- [30] P. Roux, B. Goyeau, D. Gobin, F. Fichot, M. Quintard, *Int. J. Heat Mass Transfer* 49 (2006) 4496–4510.
- [31] Y. Frautrelle, CNRS-SIMAP-EPM, France, personal communication, 2011.